Northumbria Research Link

University**Library**

A Plane Linkage and Its Tessellation for Deployable Structure

Xuesong Chen[1,2], Huijuan Feng[3], Jiayao Ma[1,2], Yan Chen[1,2]*

[1]Key Laboratory of Mechanism Theory and Equipment Design of Ministry of Education, Tianjin University, Tianjin 300072, PR China
[2]School of Mechanical Engineering, Tianjin University, Tianjin 300072, PR China
[3]Reconfigurable Robotics Lab, École Polytechnique Fédérale de Lausanne (EPFL), 1015 Lausanne, Switzerland

Abstract：

Deployable structures are widely used in space applications such as solar arrays and antennas. Recently, inspired by origami, more deployable structures have been developed. This paper outlined a novel design scheme for deployable structures by taking a plane linkage as an origami unit with a large deployable ratio. The mountain and valley (M-V) crease assignment and kinematics of the plane linkage were analyzed. Physical interference in the folding progress was discovered geometrically and resolved by the split-vertex technique. Finally, tessellation of the derived pattern was successfully used to create a large-deployable-ratio structure, which was found to exhibit considerable potential in future space applications.

Keywords：

Deployable structure; origami; plane linkage; tessellation.

1. Introduction

Origami is an ancient oriental art, which can fold two-dimensional (2D) materials into complex three-dimensional (3D) sculptures by following the designed crease patterns [1]. In the field of space engineering, origami-inspired deployable structures such as solar arrays [2] and satellite antennas [3] have to be packed into smaller volumes for transportation [4]. As many space structures are rigid when deployed, rigid origami, a branch of origami, has become the focus of research [5-7]. Rigid origami emphasizes that the facets around creases rotate without being stretched or bended during folding [8]. From a viewpoint of kinematics, creases can be considered as hinges and facets can be considered as rigid links [9-11]. Hence, the whole origami pattern can be converted into a network of mechanisms [12], and the kinematic theory can be applied to analyze the folding process and mechanical features of rigid origami [13-15]. Generally, an origami pattern contains of two types of creases called mountain and valley creases, which constrains the rotation on the mechanism joints into a half circle, i.e., $(0, \pi)$ for dihedral angles as the folding facets cannot penetrate each other after fully folded.

Many rigid origami patterns, such as Miura-ori pattern [16], Resch pattern [17], Huffman's tessellations [18] and PCCP shells [19], are tessellations of basic unit patterns [20]. Inspired by the tessellating origami patterns, large deployable structures such as solar arrays and shelters have been created [21, 22]. On the other hand, we can construct large deployable structures from seeking ideal basic origami units.

In 1942, Goldberg designed a simple origami pattern termed as a plane linkage

---

[23] as illustrated in Fig. 1, whose large deployable ratio makes it a potential construction unit for deployable structures. Yet, there was very little study on its kinematics. Therefore, this paper aims to analyze the kinematic behaviours of the plane linkage and modify it into an ideal origami unit for deployable structures.

The layout of this paper is as follows. The analysis of the M-V crease assignment and kinematics for the plane linkage are presented in section 2, followed by kinematic analysis of the equivalent 7R linkage in section 3. In section 4, the interference of the plane linkage is detected and overcome by proposing a split-vertex pattern. We design a one-DOF pattern with a large deployable ratio by tessellating the derived unit pattern in section 5. Conclusions and further discussion are given in section 6, which ends this paper.

2. Kinematics of the Plane Linkage

The plane linkage is an origami pattern with a twisted folding feature. As shown in Fig. 1(a), it consists of three regular triangular facets and five rhombus facets, of which interior angles are $\pi/3$ or $2\pi/3$. The lengths of all polygon sides are identical, and mountain and valley creases are defined as solid and dash lines, respectively. If considering creases as hinges and facets as rigid links, two spherical 4R linkages with facets 1, 8, 3, 2 and 3, 8, 5, 4 and a spherical 5R linkage with facets 1, 7, 6, 5, 8 form the whole plane linkage. Comparing the deployed and folded configurations in Fig. 1, the deployable ratio of a single plane linkage unit is 13/4.
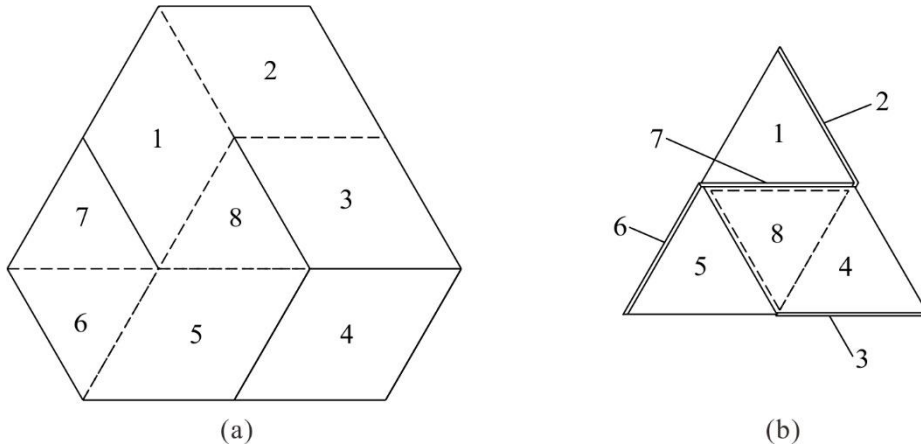

(a) (b)
Fig. 1 Two states of the plane linkage: (a) the deployed state; (b) the folded state [23]

To study the kinematics of the plane linkage, Denavit and Harternberg's (D-H) matrix method [24] is employed. D-H notation is used to describe the geometrical parameters and kinematic variables of two links, which are connected by a revolute joint as shown in Fig. 2(a). Here, $a_{i(i+1)}$ represents the length of the link. z_i is the axis of joint i and x_i is the common normal from z_{i-1} to z_i. The rotation angle between z_i and z_{i+1} is defined by $\alpha_{i(i+1)}$, positively about x_{i+1}. The rotation angle between x_i and x_{i+1} is defined by θ_i, positively about z_i. R_i, called the offset of joint i, represents the distance from x_i to x_{i+1}, positively about z_i. With the D-H matrix method in kinematics, the closure equation of a closed-loop linkage is

$$T_{12}T_{23}T_{34}...T_{(i-1)i}T_{i1} = I, \qquad (1)$$

where matrix $T_{i(i+1)}$ transforms the expression in the ($i+1$)th coordinate system to the ith coordinate system,

$$\boldsymbol{T}_{i(i+1)} = \begin{bmatrix} \cos\theta_i & -\cos\alpha_{i(i+1)}\sin\theta_i & \sin\alpha_{i(i+1)}\sin\theta_i & a_{i(i+1)}\cos\theta_i \\ \sin\theta_i & \cos\alpha_{i(i+1)}\cos\theta_i & -\sin\alpha_{i(i+1)}\cos\theta_i & a_{i(i+1)}\sin\theta_i \\ 0 & \sin\alpha_{i(i+1)} & \cos\alpha_{i(i+1)} & R_i \\ 0 & 0 & 0 & 1 \end{bmatrix}.$$

The inverse transformation can be expressed as

$$\boldsymbol{T}_{(i+1)i} = \begin{bmatrix} \cos\theta_i & \sin\theta_i & 0 & -a_{i(i+1)} \\ -\cos\alpha_{i(i+1)}\sin\theta_i & \cos\alpha_{i(i+1)}\cos\theta_i & \sin\alpha_{i(i+1)} & -R_i\sin\alpha_{i(i+1)} \\ \sin\alpha_{i(i+1)}\sin\theta_i & -\sin\alpha_{i(i+1)}\cos\theta_i & \cos\alpha_{i(i+1)} & -R_i\cos\alpha_{i(i+1)} \\ 0 & 0 & 0 & 1 \end{bmatrix}.$$

In Fig. 2(b), as the axes of spherical linkages intersect at one point, each link has no length and offset. We can simplify Eq. (1) to

$$\boldsymbol{Q}_{12}\boldsymbol{Q}_{23}\boldsymbol{Q}_{34}\cdots\boldsymbol{Q}_{(i-1)i}\boldsymbol{Q}_{i1} = \boldsymbol{I} , \tag{2}$$
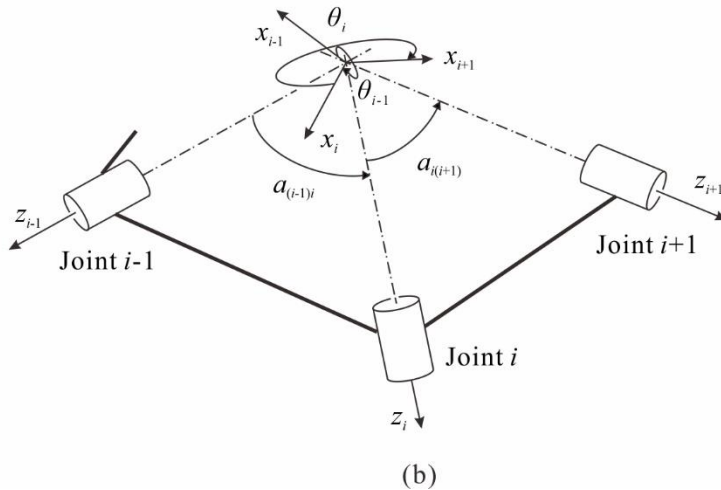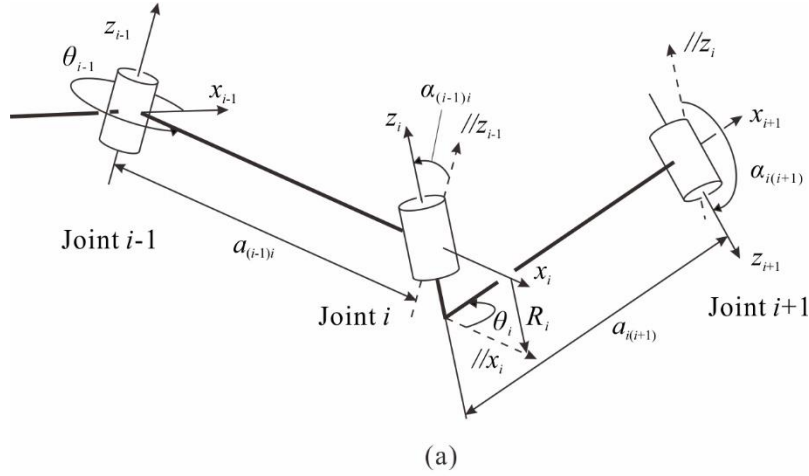
where

(a)

(b)

Fig. 2 The D-H coordinate system of (a) adjacent links connected by revolute joints (b) a portion of a spherical linkage

$$\boldsymbol{Q}_{i(i+1)} = \begin{bmatrix} \cos\theta_i & -\cos\alpha_{i(i+1)}\sin\theta_i & \sin\alpha_{i(i+1)}\sin\theta_i \\ \sin\theta_i & \cos\alpha_{i(i+1)}\cos\theta_i & -\sin\alpha_{i(i+1)}\cos\theta_i \\ 0 & \sin\alpha_{i(i+1)} & \cos\alpha_{i(i+1)} \end{bmatrix},$$

and

$$\boldsymbol{Q}_{(i+1)i} = \begin{bmatrix} \cos\theta_i & \sin\theta_i & 0 \\ -\cos\alpha_{i(i+1)}\sin\theta_i & \cos\alpha_{i(i+1)}\cos\theta_i & \sin\alpha_{i(i+1)} \\ \sin\alpha_{i(i+1)}\sin\theta_i & -\sin\alpha_{i(i+1)}\cos\theta_i & \cos\alpha_{i(i+1)} \end{bmatrix}.$$

The setup of D-H notation for each vertex in the plane linkage is shown in Fig. 3. The geometric condition of the whole unit is

$$\alpha_{18}=\alpha_{21}=\alpha_{39}=\alpha_{43}=\alpha_{5(10)}=\frac{2}{3}\pi,$$

$$\alpha_{89}=\alpha_{92}=\alpha_{9(10)}=\alpha_{(10)4}=\alpha_{87}=\alpha_{(10)8}=\alpha_{76}=\alpha_{65}=\frac{1}{3}\pi, \qquad (3)$$

$$a_{i(i+1)}=0, \ R_i=0.$$

The closure equation for the four-crease vertex A, which can be modelled as a spherical 4R linkage, is

$$\boldsymbol{Q}_{18}\boldsymbol{Q}_{89} = \boldsymbol{Q}_{12}\boldsymbol{Q}_{29}. \qquad (4)$$

There are two solutions,

$$\theta_2 = \theta_8, \theta_1 = -\theta_9, \theta_1 = 2\arctan(\frac{1}{2}\tan\frac{\theta_8}{2}) \qquad (5a)$$

and

$$\theta_2 = -\theta_8, \theta_1 = \theta_9, \theta_1 = 2\arctan(\frac{2}{-\tan\frac{\theta_8}{2}}). \qquad (5b)$$
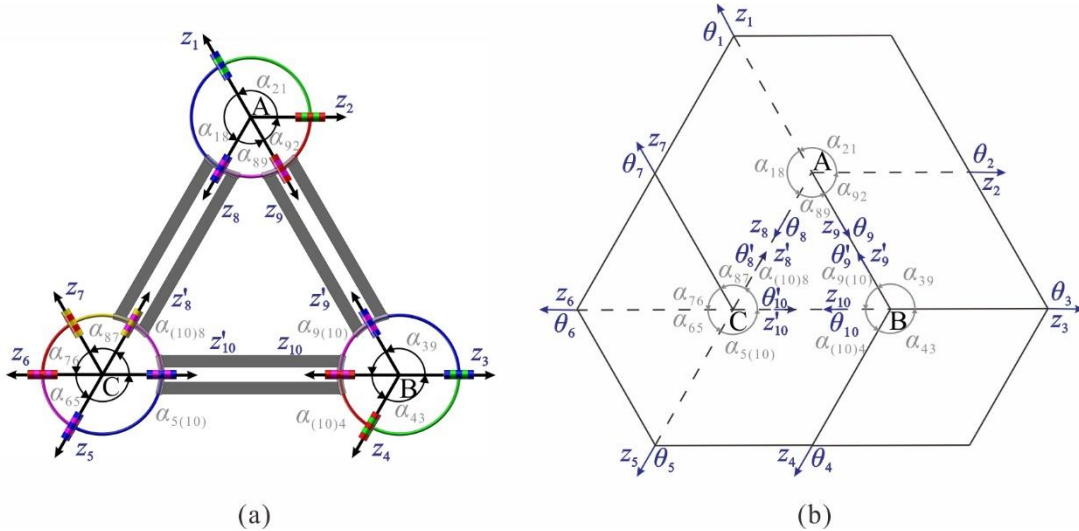

(a)　　　　　　　　　　　　　　(b)

Fig. 3 Kinematic setup of the plane linkage (a) in the linkage form; (b) in the origami pattern.

Similarly, we can also get two solutions of the spherical 4R linkage at vertex B,

$$\theta_4 = \theta_9', \theta_3 = -\theta_{10}, \theta_3 = 2\arctan(\frac{1}{2}\tan\frac{\theta_4}{2}) \qquad (5c)$$

and

$$\theta_4 = -\theta_9', \theta_3 = \theta_{10}, \theta_3 = -2\arctan(\frac{2}{\tan\dfrac{\theta_4}{2}}), \tag{5d}$$

where $\theta_9' = \theta_9$ as they are on the same crease, see Fig. 3(b). Combining Eqs. (5a-5d), there are four cases,

$$\theta_2 = \theta_8, \theta_1 = -\theta_9, \theta_4 = \theta_9, \theta_3 = -\theta_{10}, \theta_1 = 2\arctan(\frac{1}{2}\tan\frac{\theta_8}{2}), \theta_3 = 2\arctan(\frac{1}{2}\tan\frac{\theta_4}{2}), \tag{6a}$$

$$\theta_2 = \theta_8, \theta_1 = -\theta_9, \theta_4 = -\theta_9, \theta_3 = \theta_{10}, \theta_1 = 2\arctan(\frac{1}{2}\tan\frac{\theta_8}{2}), \theta_3 = -2\arctan(\frac{2}{\tan\dfrac{\theta_4}{2}}), \tag{6b}$$

$$\theta_2 = -\theta_8, \theta_1 = \theta_9, \theta_4 = \theta_9, \theta_3 = -\theta_{10}, \theta_1 = 2\arctan(\frac{2}{-\tan\dfrac{\theta_8}{2}}), \theta_3 = 2\arctan(\frac{1}{2}\tan\frac{\theta_4}{2}), \tag{6c}$$

$$\theta_2 = -\theta_8, \theta_1 = \theta_9, \theta_4 = -\theta_9, \theta_3 = \theta_{10}, \theta_1 = 2\arctan(\frac{2}{-\tan\dfrac{\theta_8}{2}}), \theta_3 = -2\arctan(\frac{2}{\tan\dfrac{\theta_4}{2}}). \tag{6d}$$

As shown in Fig. 4, θ_9 corresponds to the mountain crease AB, then we can get four M-V crease assignments at vertices A and B according to Eq. (6). Only the assignment in Fig. 4(a) meets the request that all creases move simultaneously, while the collinear creases at vertex A or B in Figs. 4(b-d) marked in red could cause that the corresponding vertex has undesired two-stage folding.
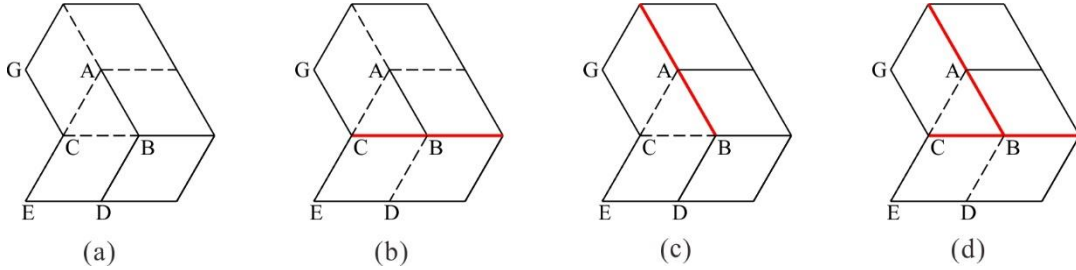

Fig. 4 Four cases of the M-V crease assignments at vertices A and B.
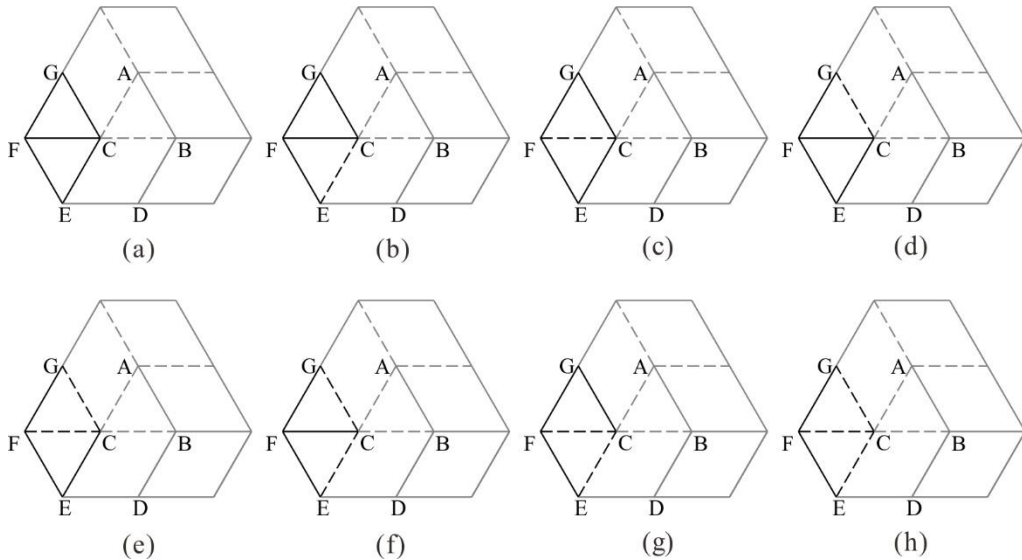

Fig. 5 The M-V crease assignments at vertex C in the plane linkage.

The kinematic relationship of linkage in Fig. 4(a) is Eq. (6a), which can be further simplified as

$$\theta_2 = \theta_8 = 2\arctan(2\tan\frac{\theta_1}{2}),$$

$$\theta_3 = -2\arctan(\frac{1}{2}\tan\frac{\theta_1}{2}),$$

$$\theta_4 = \theta_9 = -\theta_1,$$

$$\theta_{10} = 2\arctan(\frac{1}{2}\tan\frac{\theta_1}{2}).$$

(7)

Next, to explore the M-V crease assignments at vertex C, a five-crease vertex, all eight possible cases are shown in Fig. 5. After folding the card models, we found that only case (g) can be flat-foldable.

For the spherical $5R$ linkage at vertex C, $\theta_8' = \theta_8$ and $\theta_{10}' = \theta_{10}$ due to the common creases CA and CB are shared with the adjacent $4R$ linkages at vertices A and B, respectively, see Fig. 3(b). Its closure equation is

$$\boldsymbol{Q}_{78}\boldsymbol{Q}_{8(10)}\boldsymbol{Q}_{(10)5} = \boldsymbol{Q}_{76}\boldsymbol{Q}_{65}.$$

(8)

The solution for θ_5, θ_6 and θ_7 can be obtained,

$$2\sin\theta_{10}\cos\theta_5 + 2\cos\theta_8\sin\theta_{10}\cos\theta_5 + 4\sin\theta_8\cos\theta_5\cos\theta_{10} - 3\cos\theta_8\sin\theta_5 +$$
$$\sin\theta_5 - 4\sin\theta_6 - \cos\theta_{10}\sin\theta_5 - \cos\theta_8\cos\theta_{10}\sin\theta_5 + 2\sin\theta_8\sin\theta_5\sin\theta_{10} = 0,$$

$$\cos\theta_6 = \frac{1}{2} - \frac{1}{2}\cos\theta_8 + \frac{1}{2}\cos\theta_{10} + \frac{1}{2}\cos\theta_8\cos\theta_{10} - \sin\theta_8\sin\theta_{10},$$

(9)

$$2\cos\theta_8\sin\theta_{10} + \sin\theta_8\cos\theta_{10} - \sin\theta_8 - \sin\theta_7 - 2\cos\theta_7\sin\theta_6 - \sin\theta_7\cos\theta_6 = 0.$$

Equations (7) and (9) form the whole set of kinematic equations of the plane linkage in Fig. 3. We can tell that this linkage is one DOF with ten kinematic variables and nine constraints.

In origami, dihedral angles are preferred to present the folding process visually. As presented in Fig. 3(b), the relationship between the kinematic variable θ_i and the dihedral angle φ_i for the plane linkage is $\varphi_i = \pi + \theta_i$ for a mountain crease and $\varphi_i = \pi - \theta_i$ for a valley crease. For vertex A in Fig. 3, we have

$$\varphi_1 = \pi - \theta_1, \varphi_2 = \pi - \theta_2, \varphi_8 = \pi - \theta_8, \varphi_9 = \pi + \theta_9,$$

(10a)

for vertex B,

$$\varphi_3 = \pi + \theta_3, \varphi_4 = \pi + \theta_4, \varphi_{10} = \pi - \theta_{10},$$

(10b)

and for vertex C,

$$\varphi_5 = \pi - \theta_5, \varphi_6 = \pi - \theta_6, \varphi_7 = \pi + \theta_7.$$

(10c)

Finally, we obtain the motion equations of the plane linkage,

$$\varphi_2 = \varphi_8 = 2\arctan(\frac{1}{2}\tan\frac{\varphi_1}{2}),$$

(11a)

$$\varphi_4 = \varphi_9 = \varphi_1,$$

(11b)

$$\varphi_3 = \varphi_{10} = \pi - 2\arctan(\frac{1}{2}\cot\frac{\varphi_1}{2}),$$

(11c)

$$-2\sin\varphi_{10}\cos\varphi_5 + 2\cos\varphi_8\sin\varphi_{10}\cos\varphi_5 + 4\sin\varphi_8\cos\varphi_{10}\cos\varphi_5 + 3\cos\varphi_8\sin\varphi_5 +$$
$$\sin\varphi_5 - 4\sin\varphi_6 + \cos\varphi_{10}\sin\varphi_5 - \cos\varphi_8\cos\varphi_{10}\sin\varphi_5 + 2\sin\varphi_8\sin\varphi_{10}\sin\varphi_5 = 0,$$

(11d)

$$\cos\varphi_6 = -\frac{1}{2} - \frac{1}{2}\cos\varphi_8 + \frac{1}{2}\cos\varphi_{10} - \frac{1}{2}\cos\varphi_8\cos\varphi_{10} + \sin\varphi_8\sin\varphi_{10}, \quad (11e)$$

$$-2\cos\varphi_8\sin\varphi_{10} - \sin\varphi_8\cos\varphi_{10} - \sin\varphi_8 + \sin\varphi_7 + 2\cos\varphi_7\sin\varphi_6 + \sin\theta_7\cos\varphi_6 = 0. \quad (11f)$$

The relationships between φ_1 and φ_i are plotted in Fig. 6. When φ_1 changes from 0 to π, there is always $\varphi_i \geq 0$，which means that there is no kinematic interference. Once φ_1 is given, the other dihedral angles can be definitely determined, i.e., the plane linkage has one DOF.
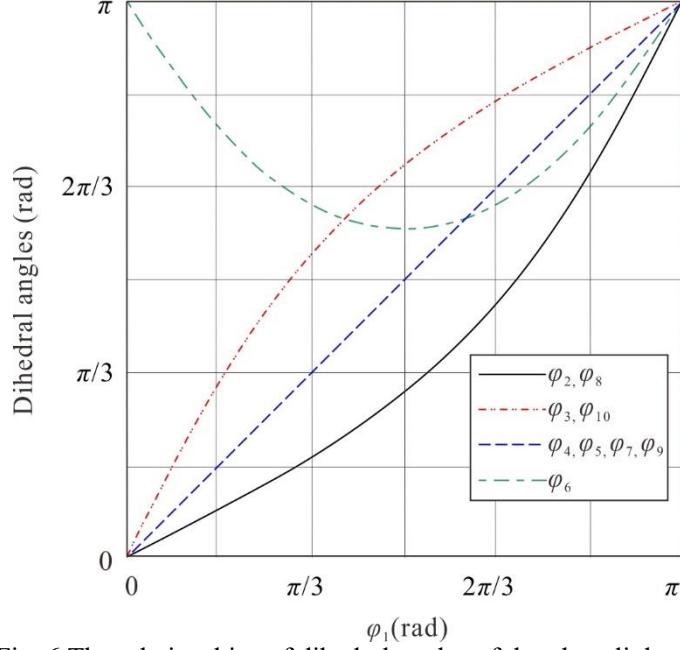

Fig. 6 The relationships of dihedral angles of the plane linkage.

3. A Derived 7*R* Linkage Based on the Plane Linkage

When the central triangular facet ABC, one of the eight facets, is cut out from the plane linkage, see Fig. 7, the remaining seven facets can be considered as a 7*R* linkage, whose kinematic parameters is setup in Fig. 8. Set the length of every side of the triangle and rhombus in Fig. 8(b) as *a*, according to the D-H notation, geometrical parameters of this 7*R* linkage are

$$a_{12}^{\gamma} = a_{34}^{\gamma} = a_{56}^{\gamma} = a_{67}^{\gamma} = 0, \ a_{23}^{\gamma} = a_{45}^{\gamma} = a_{71}^{\gamma} = \frac{\sqrt{3}}{2}a,$$

$$\alpha_{12}^{\gamma} = \alpha_{34}^{\gamma} = \frac{2}{3}\pi, \ \alpha_{56}^{\gamma} = \alpha_{67}^{\gamma} = \frac{1}{3}\pi, \ \alpha_{23}^{\gamma} = \alpha_{45}^{\gamma} = \alpha_{71}^{\gamma} = 0, \quad (12)$$

$$R_1^{\gamma} = R_3^{\gamma} = R_5^{\gamma} = R_6^{\gamma} = 0, \ R_2^{\gamma} = R_4^{\gamma} = R_7^{\gamma} = \frac{a}{2},$$

where the superscript γ represents the derived 7*R* linkage.

The closure equation of this 7*R* linkage is

$$\boldsymbol{T}_{67}\boldsymbol{T}_{71}\boldsymbol{T}_{12}\boldsymbol{T}_{23} = \boldsymbol{T}_{65}\boldsymbol{T}_{54}\boldsymbol{T}_{43} \quad (13a)$$

or

$$\boldsymbol{T}_{67}\boldsymbol{T}_{71}\boldsymbol{T}_{12} = \boldsymbol{T}_{65}\boldsymbol{T}_{54}\boldsymbol{T}_{43}\boldsymbol{T}_{32}. \quad (13b)$$
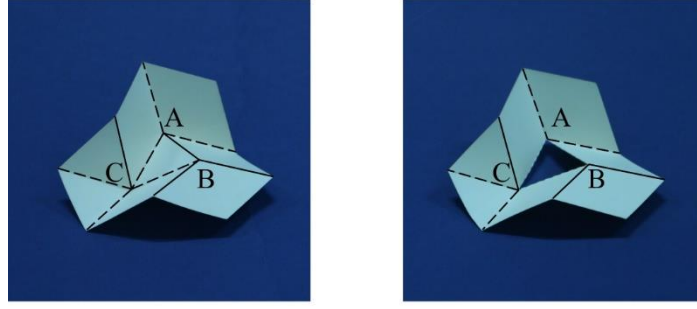
(a)   (b)

Fig. 7 The card models of (a) the plane linkage and (b) the derived 7R linkage from the plane linkage.
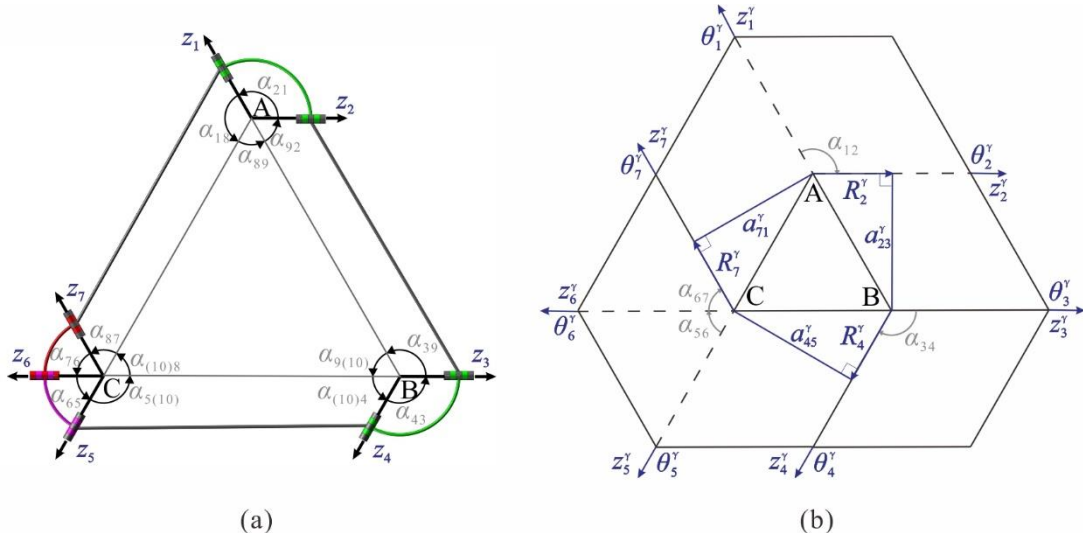
(a)   (b)

Fig. 8 Kinematic setup of the 7R linkage (a) in the linkage form; (b) in the origami pattern

Combining Eqs. (12-13), we can get the relationship between θ_1^γ and θ_i^γ,

$$\theta_3^\gamma = 2\arctan(\frac{\tan\frac{\theta_1^\gamma}{2}-3}{1-3\tan\frac{\theta_1^\gamma}{2}}), \quad \theta_4^\gamma=\theta_7^\gamma=-\theta_1^\gamma, \quad \theta_5^\gamma=\theta_1^\gamma, \quad \theta_6^\gamma=2\arctan(\frac{3}{4}\cos\theta_1^\gamma), \tag{14}$$

$$2\cos(\theta_2^\gamma-\theta_6^\gamma)=-2\cos\theta_6^\gamma\cos\theta_1^\gamma-\sin\theta_6^\gamma\sin\theta_1^\gamma+\sin\theta_6^\gamma-2\cos\theta_1^\gamma$$

as plotted in Fig. 9(a).

The relationship between the kinematic variable θ_i^γ and the dihedral angle φ_i^γ is

$$\varphi_1^\gamma=\theta_1^\gamma-\frac{\pi}{2}, \quad \varphi_2^\gamma=\theta_2^\gamma+\frac{\pi}{2}, \quad \varphi_3^\gamma=\frac{\pi}{2}-\theta_3^\gamma, \quad \varphi_4^\gamma=\frac{3\pi}{2}-\theta_4^\gamma,$$

$$\varphi_5^\gamma=\theta_5^\gamma-\frac{\pi}{2}, \quad \varphi_6^\gamma=\theta_6^\gamma-\pi, \quad \varphi_7^\gamma=\frac{3\pi}{2}-\theta_7^\gamma. \tag{15}$$

Therefore, the relationship between φ_1^γ and φ_i^γ is,

$$\varphi_3^\gamma=\frac{\pi}{2}-2\arctan\frac{\tan(\frac{\varphi_1^\gamma}{2}+\frac{\pi}{4})-3}{1-3\tan(\frac{\varphi_1^\gamma}{2}+\frac{\pi}{4})}, \tag{16a}$$

$$\varphi_4^\gamma=\varphi_5^\gamma=\varphi_7^\gamma=\varphi_1^\gamma, \tag{16b}$$

8

$$\varphi_6^\gamma = \pi - 2\arctan(\frac{3}{4}\sin\varphi_1^\gamma), \qquad (16c)$$

$$2\sin(\varphi_2^\gamma - \varphi_6^\gamma) = 2\cos\varphi_6^\gamma\sin\varphi_1^\gamma - \sin\varphi_6^\gamma\cos\varphi_1^\gamma + \sin\varphi_6^\gamma - 2\sin\varphi_1^\gamma. \qquad (16d)$$

When θ_1^γ varies from $\pi/2$ to $3\pi/2$, φ_1^γ belongs to $(0, \pi)$. As plotted in Fig. 9(b), the motion of this derived 7R linkage is identical to the plane linkage.
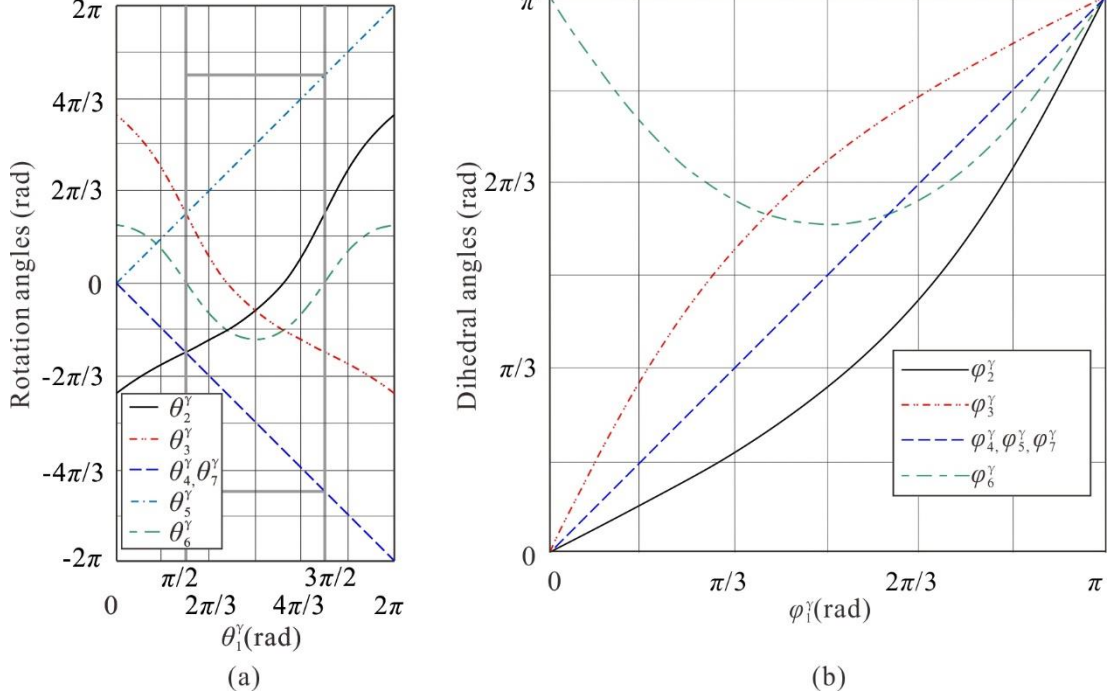

Fig. 9 The relationships of (a) rotation angles θ_i^r; (b) dihedral angles φ_i^r for the derived 7R linkage.

4. Split-vertex Technique to Avoid Physical Interference

During folding the card model of the plane linkage, physical interference occurs as intersection happens between the red creases BD and CG in Fig. 10. Such interference has to be avoided when designing a rigidly deployable structure.

In Fig. 10(b), a coordinate system is set up, whose origin is at vertex C. The y axis is set along crease CA and the z axis is perpendicular to facet 8. φ_8 is the dihedral angle between facet 1 and facet 8. φ_{10} is the dihedral angle between facet 5 and facet 8. From Eq. (11a-c), we have $\varphi_{10} = \pi - 2\arctan(\frac{1}{4}\cot\frac{\varphi_8}{2})$.
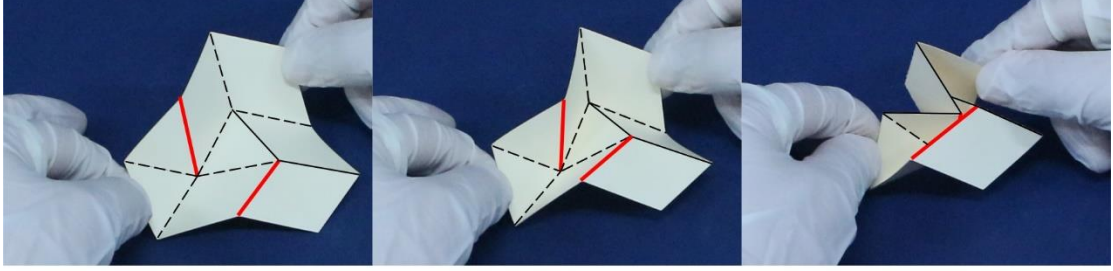
Set the length of every side of the triangle and rhombus in Fig. 10 as a, the coordinates of B, C, D and G can be represented as follows,

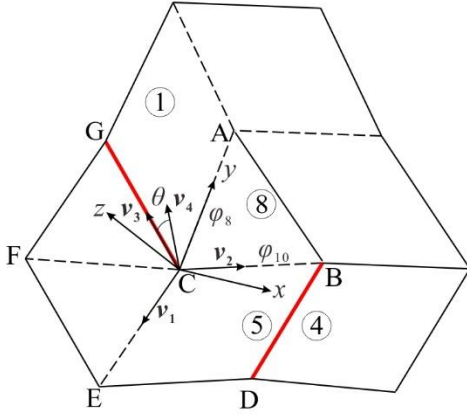$$B(\frac{\sqrt{3}}{2}a, \frac{a}{2}, 0),$$

$$C(0, 0, 0),$$

$$D(\frac{\sqrt{3}}{4}a - \frac{\sqrt{3}}{4}a\cos\varphi_{10}, \frac{a}{4} + \frac{3a}{4}\cos\varphi_{10}, \frac{\sqrt{3}}{2}a\sin\varphi_{10}), \qquad (17)$$

$$G(\frac{\sqrt{3}}{2}a\cos\varphi_8, \frac{a}{2}, \frac{\sqrt{3}}{2}a\sin\varphi_8).$$
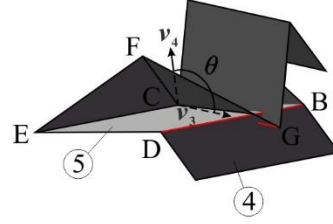
Further, we can get three vectors:

9

$$CG = (\frac{\sqrt{3}}{2}a\cos\varphi_8, \frac{a}{2}, \frac{\sqrt{3}}{2}a\sin\varphi_8),$$

$$BD = (-\frac{\sqrt{3}}{4}a - \frac{\sqrt{3}}{4}a\cos\varphi_{10}, -\frac{a}{4} + \frac{3a}{4}\cos\varphi_{10}, \frac{\sqrt{3}}{2}a\sin\varphi_{10}), \qquad (18)$$

$$CB = (\frac{\sqrt{3}}{2}a, \frac{a}{2}, 0).$$

(a)

(b)   (c)

Fig. 10 The physical interference in the plane linkage. (a) Folding of the card model; (b) the setup of the coordinate system and dihedral angles; (c) the obtuse angle θ when crease CG penetrates facet 5

To further simplify the calculation, we replace **CE**, **CB** and **CG** with their parallel vectors v_1, v_2 and v_3, respectively.

$$v_1 = (-\sqrt{3} - \sqrt{3}\cos\varphi_{10}, -1 + \cos\varphi_{10}, 2\sqrt{3}\sin\varphi_{10})$$
$$v_2 = (\sqrt{3}, 1, 0) \qquad (19)$$
$$v_3 = (\sqrt{3}\cos\varphi_8, 1, \sqrt{3}\sin\varphi_8)$$

Thus, we have the normal vector of facet 5 as

$$v_4 = v_1 \times v_2 = (-2\sqrt{3}\sin\varphi_{10}, 6\sin\varphi_{10}, -4\sqrt{3}\cos\varphi_{10}) \qquad (20)$$

and θ is the angle between vector v_3 (**CG**) and v_4,

$$\cos\theta = \frac{v_3 \cdot v_4}{|v_3| \cdot |v_4|}, \qquad (21)$$

$$k = \frac{\cos\theta}{|\cos\theta|} = \frac{v_3 \cdot v_4}{|v_3 \cdot v_4|} = \frac{-\cos\varphi_8\sin\varphi_{10} + \sin\varphi_{10} - 2\sin\varphi_8\cos\varphi_{10}}{|-\cos\varphi_8\sin\varphi_{10} + \sin\varphi_{10} - 2\sin\varphi_8\cos\varphi_{10}|}. \qquad (22)$$

As shown in Fig. 10(b-c), in the folding progress of the plane linkage, when θ is

an acute angle, no interference occurs, $k = 1$. When θ is an obtuse angle, crease CG penetrates facet 5, $k = -1$.

In three-dimensional space, the distance between creases CG and BD can be calculated as

$$d = k \cdot \frac{\left|(\boldsymbol{CG} \times \boldsymbol{BD}) \cdot \boldsymbol{CB}\right|}{\left|\boldsymbol{CG} \times \boldsymbol{BD}\right|}. \tag{23}$$

$$\frac{d}{a} = k \cdot \frac{\left|\dfrac{3}{8}\sin\varphi_{10} - \dfrac{3}{4}\sin\varphi_8\cos\varphi_{10} - \dfrac{3}{8}\cos\varphi_8\sin\varphi_{10}\right|}{\sqrt{\begin{bmatrix} (\dfrac{\sqrt{3}}{4}\sin\varphi_{10} - \dfrac{3\sqrt{3}}{8}\sin\varphi_8\cos\varphi_{10} + \dfrac{\sqrt{3}}{8}\sin\varphi_8)^2 + (-\dfrac{3}{8}\sin\varphi_8\cos\varphi_{10} - \dfrac{3}{8}\sin\varphi_8 \\ -\dfrac{3}{4}\cos\varphi_8\sin\varphi_{10})^2 + (\dfrac{3\sqrt{3}}{8}\cos\varphi_8\cos\varphi_{10} - \dfrac{\sqrt{3}}{8}\cos\varphi_8 + \dfrac{\sqrt{3}}{8}\cos\varphi_{10} + \dfrac{\sqrt{3}}{8})^2 \end{bmatrix}}} \tag{24a}$$

The relationship curve between d/a and φ_8 is plotted in Fig. 11. We can see that when φ_8 changes from 0 to 0.44 rad, the value of d/a is negative, which means that crease CG penetrates facet 5. As a result, there is physical interference during the folding.
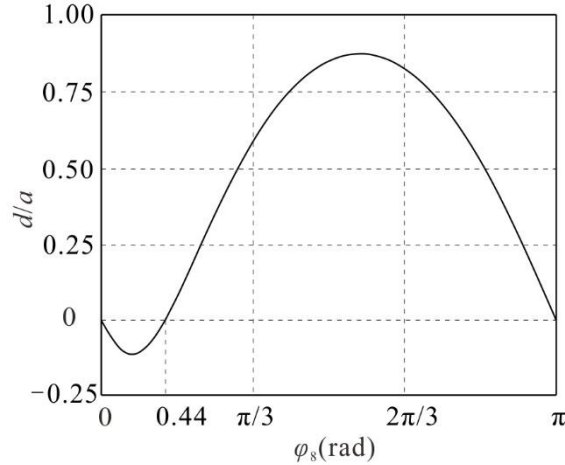

Fig. 11 The relation between d/a and φ_8

To avoid physical interference in the plane linkage, the distance between crease CG and crease BD must be increased. Here, the split-vertex technique [25, 26] is taken into consideration. In Fig. 12, we split vertex C into vertex C and vertex C′. Valley crease CF becomes valley crease CF and mountain crease C′F′, which are parallel to each other. The split distance between vertices C and C′ is l. The length of AB is extended with l correspondingly. In such a way, the plane linkage is split into a pattern with four vertices, each with four creases, and the pattern is one DOF under the overconstrained condition [27, 28].
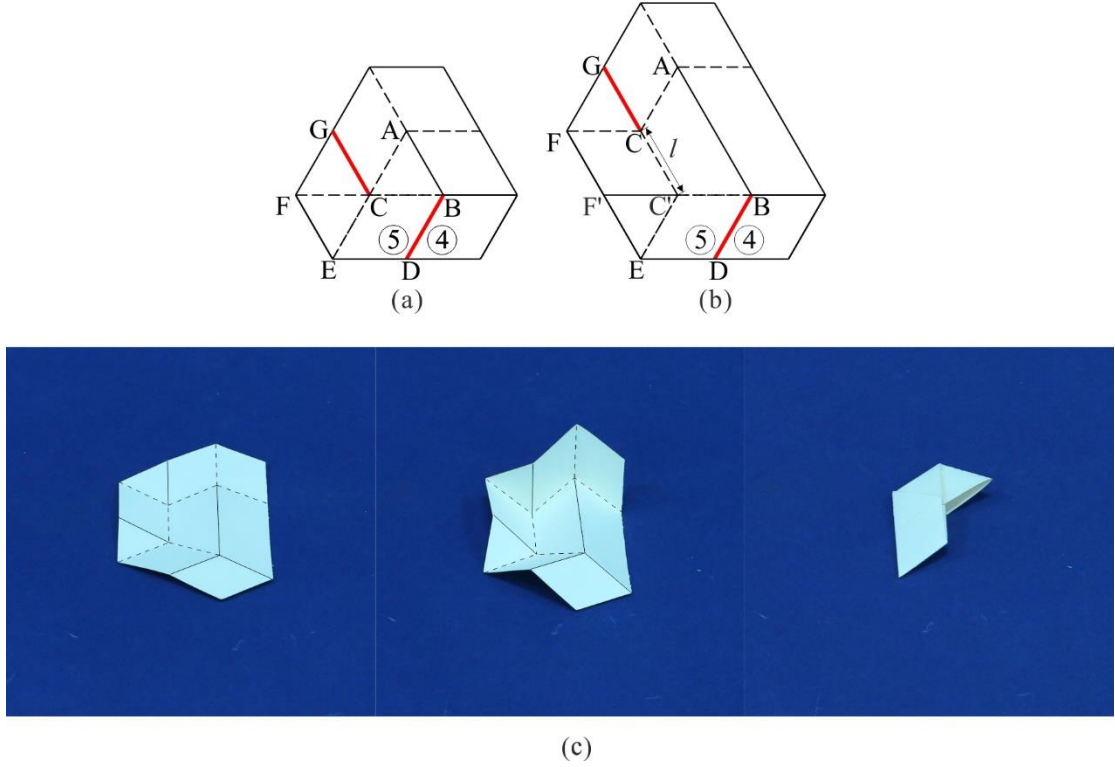
Fig. 12 The split-vertex the plane linkage: (a) the plane linkage; (b) the split pattern; (c) the card model.

The distance between CG and BD, d_l/a is related to the split distance l during the folding process,

$$\frac{d_l}{a} = k_l \cdot \frac{\left|(\frac{3}{8}+\frac{3l}{8a})\sin\varphi_{10} - (\frac{3}{4}+\frac{3l}{8a})\sin\varphi_8\cos\varphi_{10} + (\frac{3l}{8a}-\frac{3}{8})\cos\varphi_8\sin\varphi_{10} + \frac{3l}{8a}\sin\varphi_8\right|}{\sqrt{\begin{array}{c}(\frac{\sqrt{3}}{4}\sin\varphi_{10} - \frac{3\sqrt{3}}{8}\sin\varphi_8\cos\varphi_{10} + \frac{\sqrt{3}}{8}\sin\varphi_8)^2 + (-\frac{3}{8}\sin\varphi_8\cos\varphi_{10} - \frac{3}{8}\sin\varphi_8 \\ -\frac{3}{4}\cos\varphi_8\sin\varphi_{10})^2 + (\frac{3\sqrt{3}}{8}\cos\varphi_8\cos\varphi_{10} - \frac{\sqrt{3}}{8}\cos\varphi_8 + \frac{\sqrt{3}}{8}\cos\varphi_{10} + \frac{\sqrt{3}}{8})^2\end{array}}} \cdot$$

(24b)

From Fig. 11, we can infer that $d_l/a < 0$ when φ_8 is quite small and $d_l/a > 0$ when φ_8 is large enough. So there must be a certain φ_8 called φ_8^0 making $d_l/a=0$ if the split distance l is not long enough to avoid the interference. Thus we mark $k_l=-1$ when $\varphi_8 < \varphi_8^0$ and $k_l=1$ when $\varphi_8 \geq \varphi_8^0$. φ_8^0 is obtained by solving $d_l/a=0$ as

$$\tan^2\frac{\varphi_8^0}{2} = \frac{1-4l/a}{16l/a+20}.$$

(25)

When $1-4l/a > 0$, that is, $l/a < 1/4$, the solution of Eq. (25) is $\varphi_8^0 = 2\arctan\sqrt{(1-4l/a)/(16l/a+20)}$. When $l/a \geq 1/4$, no solution of Eq. (25) exists, which means that l is long enough to avoid the interference, so we mark $k_l=1$. Then the curve of d_l/a vs. φ_8 can be plotted as shown in Fig. 13.
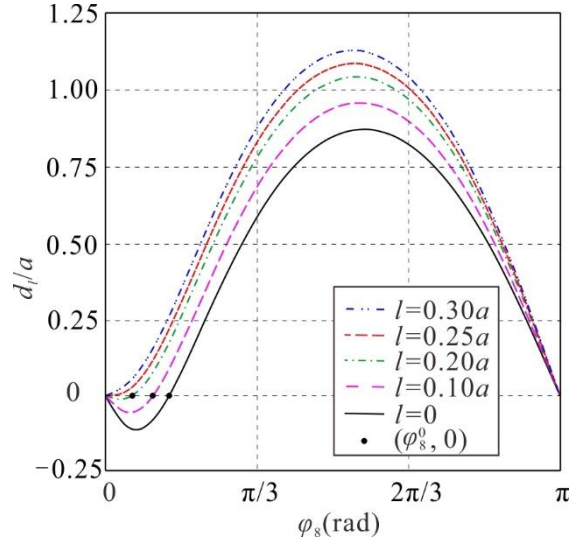
Fig. 13 The relationship between d_l/a and φ_8 with different l.

From Fig. 13, we can find that the maximum interference occurs when $l = 0$ and the interference disappears when $l \geq 0.25a$, which indicates that to avoid the interference, $l_{\min} = 0.25a$.
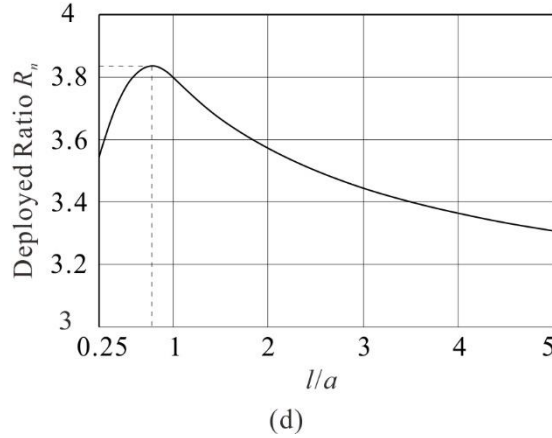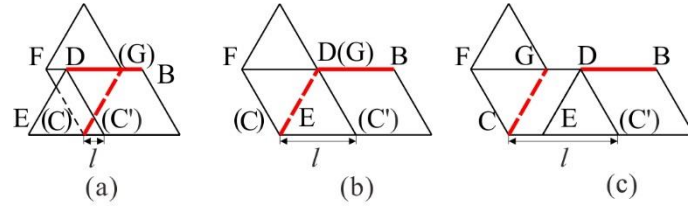

Fig. 14 The folding of the split pattern. The folded shape for different l: (a) $l_{\min} \leq l < a$; (b) $l = a$; (c) $l > a$; (d) The relationship between split distance and deployable ratio.

When the split distance l varies, the folded shape of the plane linkage changes, see Fig. 14(a-c). Thus the deployable ratio R_n also changes with l.

$$
R_n =
\begin{cases}
\dfrac{\dfrac{13\sqrt{3}}{4}a^2 + \dfrac{3\sqrt{3}}{2}a\cdot l}{\sqrt{3}a^2 + \dfrac{\sqrt{3}}{4}l^2} = \dfrac{\dfrac{6l}{a}+13}{(\dfrac{l}{a})^2+4} \left(l_{\min} \le l < a\right) \\[2em]
\dfrac{\dfrac{13\sqrt{3}}{4}a^2 + \dfrac{3\sqrt{3}}{2}a\cdot l}{\dfrac{3\sqrt{3}}{4}a^2 + \dfrac{\sqrt{3}}{2}a\cdot l} = \dfrac{\dfrac{6l}{a}+13}{\dfrac{2l}{a}+3} \qquad (l \ge a)
\end{cases}
, \qquad (26)
$$

which is plotted in Fig. 14(d). When $l = 0.78a$, the deployable ratio reaches its maximum at 3.84.

5. Tessellation of the Split Pattern

To design a hexagonal antenna, six split patterns can be tessellated into a large pattern with Miura-ori as the intermediate connection, see Fig. 15. Due to the compatibility between the split pattern and Miura-ori, the whole pattern presented in Fig. 15(a) has a single DOF.
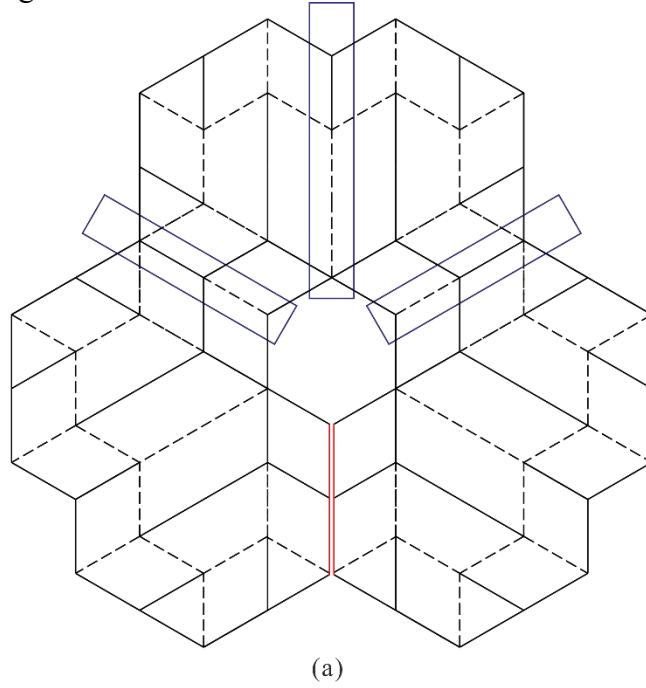

(a)

(b)

Fig. 15 Tessellation of the split pattern. (a) The pattern formed by six split patterns (no creases between red lines); (b) the card model of it.

To make a fully covered hexagon, the pattern is further modified by filling the gaps around the edge, see Fig. 16(a). The folding sequence of such a card model is presented in Fig. 16(b). It can be found that the deployable ratio of this structure is 30/1.

It should be noted that the change of cutting position, shown by the red lines in Fig. 16(a), does not affect the DOF of the regular hexagon pattern. Because the patterns in the blue frames beside the cutting position can be considered as two one-DOF Miura-ori patterns.

(a)
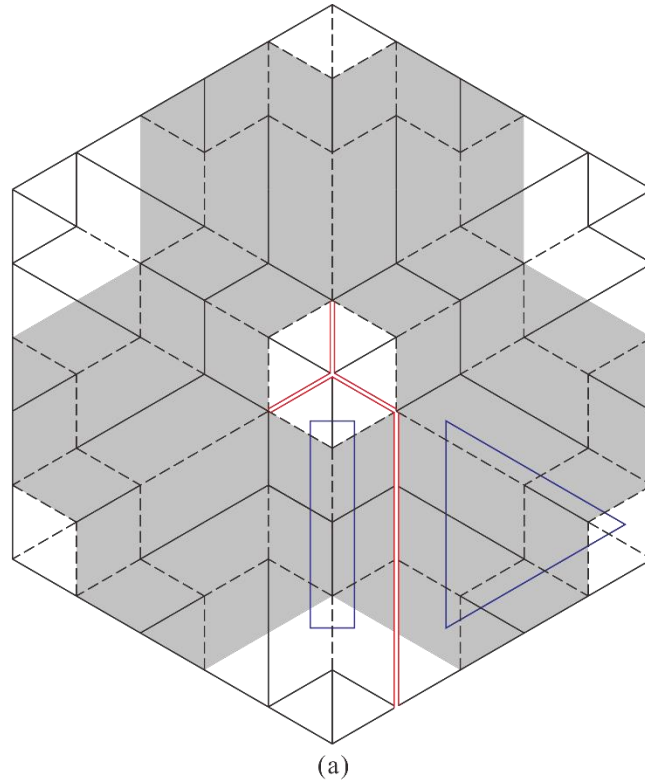
(b)

Fig. 16 The regular hexagon pattern. (a) Improvement of the tessellation (no creases between red lines); (b) its folding sequence.

6. Conclusions

In this paper, a plane linkage with a twisted folding feature is used as the basic origami unit to design a large deployable structure with a large deployable ratio. The kinematics of the unit has been studied from the viewpoint of a rigid origami pattern and a derived $7R$ linkage. To avoid physical interference, a split pattern with 4-crease vertices has been proposed, and a tessellation of this unit was designed to achieve a

large deployable ratio and single DOF. Card models have been made to validate the study.

To bring this work into application in the future, the physical thickness of panels has to be considered and the control strategy for deployment will be studied. Meanwhile, other tessellations of the plane linkage and split patterns should be explored to design deployable structures with more general geometric shape besides hexagon.

Acknowledgments

Reference

[1] M. Bern, B. Hayes, The complexity of flat origami, in: Proceedings of the 7th annual ACM–SIAM symposium on discrete algorithms, Philadelphia, USA, 1996. pp. 175–83.

[2] K. Miura, Method of packaging and deployment of large membranes in space, in: Proceedings of 31st International Astronautical Federation Congress, Tokyo, 1980. Paper no. IAF–80–A31.

[3] S.A. Zirbel, R.J. Lang, M.W. Thomson, D.A. Sigel, P.E. Walkemeyer, B.P. Trease, S.P. Magleby, L.L. Howell, Accommodating thickness in origami-based deployable arrays, J. Mech. Des., 135 (2013) 111005.

[4] G. Kiper , E. Soylemez , Deployable space structures, in: 2009 4th International Conference on Recent Advances in Space Technologies, Istanbul, Turkey, 2009, pp. 131–138.

[5] K. Miura, Triangles and quadrangles in space, in: Proceedings of the International Association for Shell and Spatial Structures (IASS) Symposium, Valencia, Spain, 2009, pp. 27-38.

[6] T.U. Lee, J.M. Gattas, Geometric design and construction of structurally stabilized accordion shelters, J. Mech. Rob., 8 (2016) 031009.

[7] A. Pagano, T. Yan, B. Chien, A. Wissa, S. Tawfick, A crawling robot driven by multi-stable origami, Smart Mater. Struct., 26 (2017) 094007.

[8] N. Watanabe, K. Kawaguchi, The method for judging rigid foldability, in: Proceedings of 4th International Conference on Origami in Science, Mathematics, and Education, Pasadena, USA, 2009, pp. 165–174.

[9] J.S. Dai, J.R. Jones, Mobility in Metamorphic Mechanisms of Foldable/Erectable Kinds, Journal of Mechanical Design, 121 (1999) 375-382.

[10] J.S. Dai, J.R. Jones, Matrix Representation of Topological Changes in Metamorphic Mechanisms, Journal of Mechanical Design, 127 (2005) 837-840.

[11] E. Demaine, J. O'Rourke, Geometric Folding Algorithms: Linkages, Origami, Polyhedra2007, Boston: Cambridge University Press, 2007.

[12] M. Trautz, A. Künstler. Deployable folded plate structures-folding patterns based on 4-fold-mechanism using stiff plates, in: Proceedings of the International Association for Shell and Spatial Structures (IASS) Symposium, Valencia, Spain, 2009, pp. 2306–2317.

[13] J.S. Dai, J.R. Jones, Kinematics and mobility analysis of carton folds in packing manipulation based on the mechanism equivalent, Proceedings of the Institution of Mechanical Engineers, Part C: Journal of Mechanical Engineering Science, 216 (2002) 959-970.

[14] G. Wei, J.S. Dai, Origami-Inspired Integrated Planar-Spherical Overconstrained Mechanisms, Journal of Mechanical Design, 136 (2014) 051003.

[15] C. Qiu, V. Aminzadeh, J.S. Dai, Kinematic and Stiffness Analysis of an Origami-Type Carton, Journal of Mechanical Design, 135 (2013) 111004.

[16] S. Liu, G. Lu, Y. Chen, Y.W. Leong, Deformation of the Miura-ori patterned sheet, Int. J. Mech. Sci., 99 (2015) 130-142.

[17] T. Tachi, Designing freeform origami tessellations by generalizing Resch's patterns, J. Mech. Des., 135 (2013) 111006.

[18] E. Davis, E.D. Demaine, M.L. Demaine, J. Ramseyer, Reconstructing David Huffman's origami tessellations, J. Mech. Des., 135 (2013) 111010.

[19] K. Miura, Proposition of pseudo-cylindrical concave polyhedral shells, ISAS Rep.,34(1969) 141–163.

[20] Z. You, Y. Chen, Motion structures: deployable structural assemblies of mechanisms, London, UK: Spon Press, 2012.

[21] S.A. Zirbel, M.E. Wilson, S.P. Magleby, L.L. Howell, An Origami-Inspired Self-Deployable Array,

ASME 2013 Conference on Smart Materials, Adaptive Structures and Intelligent Systems Snowbird, USA, 2013, V001T001A026.

[22] K. Giesecke, Deployable structures inspired by the origami art, Massachusetts Institute of Technology, 2004.

[23] M. Goldberg, Polyhedral linkages, Natl. Math. Mag., 16 (1942) 323-332.

[24] J. Denavit, R.S. Hartenberg, A kinematic notation for lower-pair mechanisms based on matrices, Trans. ASME J. Appl. Mech. 22 (1955) 215–221.

[25] K.A. Tolman, R.J. Lang, S.P. Magleby, L.L. Howell, Split-vertex technique for thickness-accommodation in origami-based mechanisms, ASME 2017 Inter- national Design Engineering Technical Conferences and Computers and Information in Engineering Conference Ohio, USA, 2017 V05BT08A054.

[26] T.C. Hull, T. Tachi, Double-line rigid origami, arXiv preprint, (2017) arXiv:1709.03210.

[27] T.A. Evans, R.J. Lang, S.P. Magleby, L.L. Howell, Rigidly foldable origami twists, in: Proceedings of the 6th International Conference on Origami in Science, Mathematics, and Education, Tokyo, JAPAN, 2016, pp. 119–130.

[28] S. Liu, Y. Chen, G. Lu, The rigid origami patterns for flat surface, ASME 2013 International Design Engineering Technical Conferences and Computers and Information in Engineering Conference Portland, OR, 2013 V06BT07A039.